Seismic imaging of the shallow crust beneath the Krafla central volcano, NE Iceland

Juerg Schuler[1,2], Tim Greenfield[1], Robert S. White[1,3], Steven W. Roecker[4], Bryndís Brandsdóttir[3], Joann M. Stock[2], Jon Tarasewicz[1,5], Hilary R. Martens[2], and David Pugh[1]

[1]Bullard Laboratories, University of Cambridge, Cambridge, UK, [2]Seismological Laboratory, California Institute of Technology, Pasadena, California, USA, [3]Science Institute, University of Iceland, Reykjavík, Iceland, [4]Rensselaer Polytechnic Institute, Troy, New York, USA, [5]Now at BP, Sunbury on Thames, UK

Abstract We studied the seismic velocity structure beneath the Krafla central volcano, NE Iceland, by performing 3-D tomographic inversions of 1453 earthquakes recorded by a temporary local seismic network between 2009 and 2012. The seismicity is concentrated primarily around the Leirhnjúkur geothermal field near the center of the Krafla caldera. To obtain robust velocity models, we incorporated active seismic data from previous surveys. The Krafla central volcano has a relatively complex velocity structure with higher P wave velocities (V_p) underneath regions of higher topographic relief and two distinct low-V_p anomalies beneath the Leirhnjúkur geothermal field. The latter match well with two attenuating bodies inferred from S wave shadows during the Krafla rifting episode of 1974–1985. Within the Leirhnjúkur geothermal reservoir, we resolved a shallow (−0.5 to 0.5 km below sea level; bsl) region with low-V_p/V_s values and a deeper (0.5–1.5 km bsl) high-V_p/V_s zone. We interpret the difference in the velocity ratios of the two zones to be caused by higher rock porosities and crack densities in the shallow region and lower porosities and crack densities in the deeper region. A strong low-V_p/V_s anomaly underlies these zones, where a superheated steam zone within felsic rock overlies rhyolitic melt.

1. Introduction

Iceland sits on an insular shelf that straddles the Mid-Atlantic Ridge. The axial rift zones traversing Iceland (Figure 1, inset A) are characterized by active volcanism and faults and mark the present plate boundary between the North American and Eurasian plates. They are part of the neovolcanic zone [*Sæmundsson*, 1979]. The Northern Volcanic Zone (NVZ) is a segment of the neovolcanic zone that became an active rift segment about 6–7 Myr ago after the Reykjanes-Langjökull rift zone jumped about 130 km eastward [*Sæmundsson*, 1974; *Jancin et al.*, 1985]. Today, the NVZ links to the Kolbeinsey Ridge via the Tjörnes fracture zone offshore northern Iceland. Five elongated en échelon segments or volcanic systems are gathered in the NVZ, in the order from north to south: Þeistareykir, Krafla, Fremrinámar, Askja and Kverkfjöll. Each system comprises NNE trending fissure swarms that transect their central volcanoes approximately perpendicular to the spreading direction [*Hjartardóttir et al.*, 2015]. Exposed rocks in the rift zones are mostly basaltic, with a smaller volume of more evolved rocks confined to the central volcanoes [*Sæmundsson*, 1979]. The Krafla, Askja, and Kverkfjöll volcanoes represent relatively mature systems that have developed caldera structures in association with shallow crustal magma chambers.

Petrological analyses of erupted rocks suggest that crystallization of basalts and mixing of melts occur over a range of depths in the Icelandic crust and possibly in the uppermost mantle [e.g., *Maclennan*, 2008; *Sigmarsson et al.*, 2008]. For example, some extrusives at Þeistareykir exhibit a more olivine-tholeiitic composition probably derived directly from mantle-sourced melts [*Winpenny and Maclennan*, 2014] while other volcanic systems contain rhyolites likely originating from crustal magma chambers [*Grönvold*, 1976].

1.1. The Krafla Volcanic System

The Krafla volcanic system consists of a 100 km long and mostly 5–8 km wide fissure swarm that transects the Krafla central volcano [*Sæmundsson*, 1991; *Hjartardóttir et al.*, 2012]. The volcano extends over an area of 21 km by 17 km and exhibits relatively low relief (300–500 m elevation), as is common for central volcanoes [*Einarsson*, 2008], but with some hyaloclastic table mountains and rhyolitic ridges that reach 800 m above sea level. The age of the volcano is thought to be at least 0.5–1.8 Myr based on K/Ar and paleomagnetic
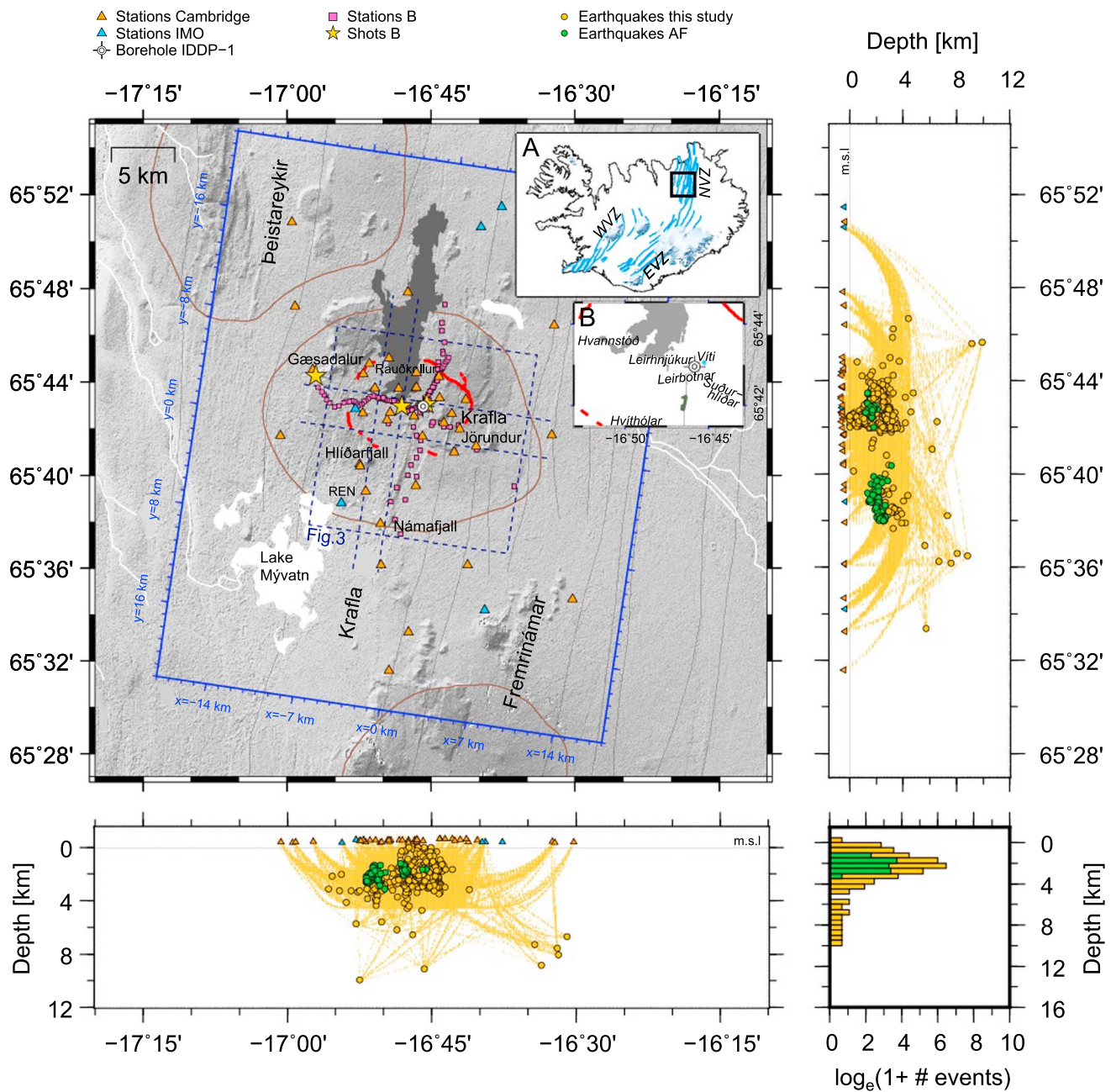
Figure 1. Map of the study area in Iceland showing the local extent of the Fremrinámar, Krafla, and Þeistareykir fissure swarms (black lines), central volcanos (brown lines), lava flows from the 1975 to 1984 Krafla fires (dark gray), mapped caldera rim (red lines), and the locations of the cross sections in Figure 3 as dashed blue lines. Inset A shows a regional map of Iceland with its main glaciers and rifting zones (blue): NVZ-Northern Volcanic Zone; WVZ-Western Volcanic Zone; EVZ-Eastern Volcanic Zone. Inset B is an enlarged map of the caldera. Descriptions of the symbols are listed in the legend at the top where the letters "B" and "AF" stand for data taken from *Brandsdóttir et al.* [1997] and *Arnott and Foulger* [1994], respectively. Outline of our grid is superimposed in blue with local coordinates used in our tomographic inversion. The hypocenter locations and ray paths from the manually picked earthquakes are shown after the first iteration of the tomographic inversion and displayed in two cross sections on the sides of the map. A histogram of the earthquake depth distribution is given at the bottom right (yellow) together with the final earthquake hypocenters from *Arnott and Foulger* [1994] (green).

dating as well as on interpretations of the underlying crustal structure from seismic imaging, with a current half-spreading rate of 9 mm/yr [*Brandsdóttir et al.*, 1997]. On the eastern and western flanks of the volcano, low-angle dipping lava flows and breccia suggest the prior existence of a shield volcano [*Björnsson et al.*, 1977]. Its elliptical caldera (10 km by 7 km) was formed about 110 kyr ago during the last interglacial period by a semiacidic eruption [*Sæmundsson*, 1982].

The geological structure of the eastern and southeastern caldera has been interpreted based on drill cuttings from geothermal boreholes [*Ármannsson et al.*, 1987]. In the Hvíthólar geothermal field (Figure 1, inset B), a 1500–1600 m thick sequence of hyaloclastite and lavas overlies basaltic intrusions. In the central geothermal production field and to the east (Leirbotnar-Suðurhlíðar), hyaloclastite and lavas are dominant to a depth of about 1000 m below the surface or 500 m below sea level (bsl), and are underlain by basaltic intrusives. To the east of Suðurhlíðar, gabbroic intrusives become more dominant at 1200–1300 m depth bsl.

Since the last glacial period 35 eruptions have been identified within the Krafla volcanic system using tephra deposits [*Björnsson et al.*, 1977, 1979]. The Mývatn fires (1724–1729) and Krafla fires (1974–1985) are two documented rifting episodes. The latter underwent 20 rifting events of which 9 resulted in basaltic fissure eruptions [*Einarsson*, 1991; *Buck et al.*, 2006]. Altogether, the 20th century rifting episode caused about 8 m horizontal extension in the central 2–3 km of the caldera [*Wendt et al.*, 1985; *Hollingsworth et al.*, 2012]. Based on the propagation pattern of the earthquake activity, magma is inferred to have been stored in the shallow crust and intermittently injected into dikes, traveling at typically 0.5 m/s along the fissure swarms [*Brandsdóttir and Einarsson*, 1979; *Wright et al.*, 2012]. Since the rifting episode, inflation and related seismic activity within the Krafla caldera have ceased. Most of the current seismicities are linked with high-temperature geothermal processes within two shallow geothermal fields [e.g., *Arnott and Foulger*, 1994; *Parker*, 2012].

Associated with central volcanoes are high-temperature geothermal fields, where faults and fissures transecting the volcanoes allow water to easily penetrate the shallow hot crust. The Krafla-Leirhnjúkur field (15 km^2) is located inside the Krafla caldera. Exploration drilling began in 1974 and the Krafla power plant started operation in 1977. Drill cuttings from wells have been used to study the mineral alteration and to construct temperature profiles of the geothermal reservoir. Most wells reach a temperature of 240°C at 1500 m depth bsl [*Halldórsdóttir et al.*, 2010].

The exposure of rhyolitic domes and ridges (e.g., Hlíðarfjall) near the caldera rim suggests that the Krafla volcano has had crustal magma chambers in the past. *Jónasson* [1994, 2007] suggested that these rhyolites are generated at the sides of an active basaltic magma chamber by near-solidus fractionation of hydrothermally altered crust. Some rhyolitic melts are known to have erupted effusively through dikes to the surface and under ice in the past, and they form ridges more than 2 km long and up to 300 m high [*Jónasson*, 1994; *Tuffen and Castro*, 2009], indicating that the underlying magma chambers were large enough to produce silicic magma.

In spring of 2009 the exploration well IDDP-1, located close to the 1724 AD Víti explosion crater (Figure 1, inset B), penetrated rhyolitic magma at 2104 m depth (1551 m bsl). Petrochemical and isotopic analyses of the recovered rock cuttings confirm that the rhyolitic melts originated from partially molten and hydrothermally altered crust [*Elders et al.*, 2011; *Zierenberg et al.*, 2012]. Quenched silicic glasses were retrieved in well KJ-39 at a similar depth [*Mortensen et al.*, 2010], with some chemical differences to the glasses in IDDP-1 which may point toward a more localized feature. Below, we refer to depth as true vertical depth below sea level if not explicitly specified.

1.2. Geophysical Studies of the Krafla Central Volcano

The depth of the crust-mantle boundary is constrained by active seismic reflections and teleseismic receiver functions to be 19–21 km depth beneath the Krafla central volcano [*Brandsdóttir et al.*, 1997; *Darbyshire et al.*, 2000]. A shallow magma chamber was inferred to sit on top of a 40 km wide high-velocity dome, extending from the lower crust [*Brandsdóttir et al.*, 1997]. The dome most likely represents gabbroic cumulates [*Brandsdóttir and Menke*, 2008]. Magnetotelluric (MT) measurements show decreasing apparent resistivities below 4–5 km depth under the Krafla caldera as well as a continuous, low-resistivity layer below 8–10 km depth [*Beblo et al.*, 1983; *Björnsson*, 1985], possibly indicating zones of increased temperature.

Shear wave attenuation studies based on inflation-induced earthquakes recorded during the beginning of the rifting episode were interpreted to outline a magma chamber with horizontal dimensions of approximately 2 km by 7 km with its top at 2.5 km depth bsl [*Einarsson*, 1978]. Most earthquakes were located above the shadow zone and were interpreted to be caused by the stress changes induced during inflation/deflation periods of the magma chamber. Few earthquakes were recorded between 4 and 8 km depth, probably due to viscoelastic rock properties [*Einarsson*, 1978; *Brandsdóttir and Einarsson*, 1979; *Einarsson*, 1991]. *Brandsdóttir and Menke* [1992] further analyzed the waveforms of the earthquakes. They resolved a low-velocity zone (LVZ)

in the northern caldera. Reflections from beneath this LVZ suggest that the magma chamber is less than 1 km thick in this region and has its top at about 2.5 km depth bsl.

A 3-D tomographic image of the shallow *P* wave velocity structure at Krafla was first obtained by *Arnott and Foulger* [1994]. They imaged high-velocity bodies in a ring-like structure beneath the caldera rim, which they interpreted as intrusions along the caldera ring fault. *Arnott and Foulger* [1994] also imaged several low-velocity anomalies inside the caldera, interpreted to represent volumes of geothermally altered rocks. *Parker* [2012] imaged a body of low *P* wave velocities (V_p) and low V_p/V_s ratio beneath the center of the caldera, thought to represent gas-filled fractures and pores in the rock and a high-velocity body beneath Leirbotnar, interpreted as a gabbroic intrusion at shallow (<2 km bsl) depth.

Gravity data further indicate a broad gravity high associated with the Krafla central volcano, extending to shallower depths beneath the caldera rims, separating a buried inner caldera and a WNW-ESE trending transform graben filled with hyaloclastite [*Árnason et al.*, 2009]. Rhyolitic domes near the caldera rims have relatively low-average rock densities (1600–1900 kg m^{-3}) [*Ágústsdóttir et al.*, 2011]. A 5 km wide elliptical deformation area within the Krafla caldera close to IDDP-1 has been interpreted as a shallow deflating magma reservoir [*Rymer et al.*, 1998; *Metzger et al.*, 2013; *Ali et al.*, 2014], in agreement with observed postrifting deflation [*Sigmundsson et al.*, 1997].

Electrical methods have also proved useful for mapping geothermal areas in Iceland. The apparent resistivity of the rocks may be affected by temperature, by chemical composition, and by water and melt fractions in the rock [e.g., *Constable*, 2006]. It was found that the resistivity is strongly affected by the dominant mineral alteration in geothermal areas, which are mainly caused by geothermal fluids [*Árnason et al.*, 2008]. Since mineral alteration can be largely predicted by temperature, the mineral compositions are used to interpret reservoir temperatures, assuming that the temperature and mineral alteration are in equilibrium. Joint inversions of MT and transient electromagnetic soundings by *Árnason et al.* [2009] show low-resistivity bodies at 2 km bsl. At greater depths, low-resistivity structures are often interpreted as zones of increased temperature, possibly caused by partial melts [*Árnason et al.*, 2009].

The model of *Brandsdóttir et al.* [1997], constructed using refraction data, shows decreased near-surface velocities and fewer lateral heterogeneities compared to the model of *Arnott and Foulger* [1994] in the uppermost 2.5 km of the Krafla caldera. Near the surface (30–100 m), *P* wave velocities were found as low as 1.1–1.8 km/s [*Zverev et al.*, 1980; *Brandsdóttir et al.*, 1997]. Unsurprisingly, the refraction data acquired with the denser receiver array allowed for better resolution of near-surface velocities and simple subhorizontal layers to about 1 km depth, consistent with borehole data [*Ármannsson et al.*, 1987].

Here we use earthquakes with epicenters in both the Þeistareykir and Krafla volcanic systems to examine the velocity structure beneath the Krafla central volcano. The aim of this study was to constrain the regions of possible melt accumulation and the properties of the active geothermal areas.

2. Data Description

The seismicity of the Námafjall-Krafla-Þeistareykir area was recorded by a seismic array of up to 31 three-component seismometers in the period from August 2009 to July 2012 (Figure 1). Four seismometers, mostly LE-3D/5s sensors on concrete plinths, were part of the permanent seismic network operated by the Icelandic Meteorological Office (IMO). Our temporary array comprised 27 Guralp CMG-6TD (30 s-50 Hz) and one CMG3-ESP broadband (60 s-50 Hz) sensors, mostly buried 0.5 m beneath the surface. Sand was used to pack and position the sensors in the ground. On average, 25 stations were active and recorded high-quality waveforms while others were exchanged, for example, due to sensor damage. The array is densest in the center of the caldera with an average spacing of 1.5–1.8 km but coarser outside.

Sparse vegetation and little human habitation in the NVZ minimize the impact of wind-induced and cultural noise, allowing us to record small earthquakes. The ground is frozen and covered by snow during the winter providing good sensor coupling but also increased risks of data loss due to power outages. Seismometer recordings near production wells showed higher noise levels than recordings from outside the geothermal fields. We recorded earthquakes in the NVZ with local magnitudes down to about −1, but mostly used earthquakes with magnitudes above −0.3 for the analysis, which typically have source dimensions of up to a few tens of meters [*Wyss and Brune*, 1968].
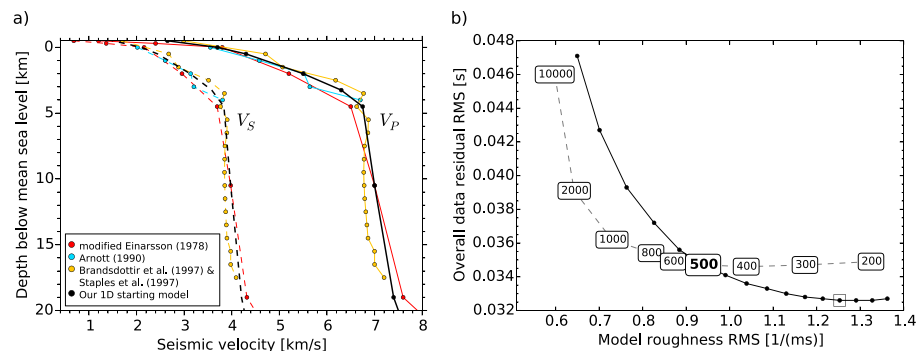
Figure 2. (a) Velocity profiles obtained in the Krafla region. Solid lines represent results obtained from data inversions, and dashed lines show the corresponding velocities inferred from a constant V_p/V_s ratio. Red [*Einarsson*, 1978]; blue [*Arnott and Foulger*, 1994]; yellow [*Brandsdóttir et al.*, 1997; *Staples et al.*, 1997]; and black, our 1-D starting model. (b) Trade-off curve (dashed line) between model roughness of the imposed model perturbations and overall data residuals when applying different damping factors (marked in boxes) during the data inversion. Values were evaluated after six iterations. The solid line shows the data misfit as a function of the inversion iteration (dots) and model roughness using a damping factor of 500. After about 13 iterations (square), no significant residual reduction is achieved without adding structural complexity to our model.

Initial detection and location of earthquakes were achieved by using the coalescence microseismic mapping (CMM) algorithm, which is based on the Bayesian inversion of arrival times of packets of high-amplitude energy [*Drew et al.*, 2013]. In this technique, a short- to long-term average onset function is calculated continuously from the vertical and combined horizontal components with a maximum in the onset function representing a likely seismic arrival time. The energy (magnitude of the onset functions) from each seismometer is migrated back into the subsurface. Peaks in this "coalescence" function represent likely hypocenter locations and origin times.

We constructed a velocity profile by averaging the models obtained by *Einarsson* [1978], *Arnott and Foulger* [1994], *Brandsdóttir et al.* [1997], and *Staples et al.* [1997] within the central 25 km of the Krafla volcano (Figure 2a), using a constant V_p/V_s ratio of 1.76. The models mainly differ at shallow depth and below 6 km. Station weighting is introduced by the onset function, i.e., signal-to-noise ratio (SNR), and location errors are reduced by integrating the coalescence function in the subsurface over the range of estimated arrival time errors. The maximum of the spatiotemporal map returns the most probable location and arrival times of an event. A total of 325,083 triggered events was identified automatically and further filtered by the SNR value and location error estimate. Four thousand, nine hundred and nine events had an average SNR value greater than 3 at all receivers. We removed events very close to the surface as well as regional events, because they are poorly located or lie outside our study area.

Several earthquakes, automatically located by CMM below 4 km depth bsl, were characterized by noisy or emergent arrivals, which are difficult to pick and lead to unreliable hypocenter depths. Therefore, we manually refined the arrival times of 1453 events by visual inspection and assigned picking errors of 0.01 s, 0.02 s, 0.05 s, 0.1 s, or 0.2 s to the *P* wave and the earliest arriving *S* waves. Hypocenters were then relocated using the probabilistic earthquake location algorithm NonLinLoc [*Lomax et al.*, 2000, 2009]. Only events with horizontal and vertical hypocenter location errors of less than 1 km were included in the analysis. From this array, 16,638 *P* wave and 8137 *S* wave phase picks were prepared for the tomographic inversion.

Relocation of the earthquakes (Figure 1) shows that the seismicity is largely confined to the upper 2.5 km of the geothermal system at Krafla. The earthquake distribution limits our resolving capabilities for much deeper structures so we decided to incorporate active and passive seismic data from previous studies. We use traveltime data from the active seismic surveys in 1993 and 1994 recorded by *Brandsdóttir et al.* [1997], where six shots, giving 173 *P* wave phases, were fired at Víti (Krafla), Gæsadalur, and Leirhnjúkur (Figure 1).

3. Three-Dimensional Tomographic Inversion

We use a 3-D tomographic inversion code developed by *Roecker et al.* [2006] to obtain velocity (V_p and V_p/V_s) models beneath Krafla. Traveltimes and ray paths are calculated by a finite-difference eikonal solver developed by *Vidale* [1988] and adapted to 3-D by *Hole and Zelt* [1995]. The solver provides high-accuracy traveltimes

and ray paths by reducing the risk of stagnating in a local traveltime minimum, in a heterogeneous velocity medium, and media that include shadow zones.

Fine and coarse grids are specified, where the fine grid has a relatively small constant spacing. The center of the local grid (x,y) = (0 km, 0 km) is set at (latitude,longitude) = (65.69200,−16.76452). P and S wave slowness and their ratios are calculated at each fine-grid node, while other points are calculated by trilinear interpolation. Contributions of the fine points are then summed to form a representative coarse-grid node. Once the traveltime table has been prepared between all node station pairs, the ray paths are determined by following the steepest traveltime gradients. Model perturbations are found by simultaneously solving for hypocenter location and slowness using a least squares solver by *Paige and Saunders* [1982]. The model and hypocenter locations are updated iteratively until the variance in data misfit is reduced significantly. A damping parameter is introduced to regularize the mix-determined inverse problem, because some cells are well covered by rays and others are not. Furthermore, the model is smoothed after every iteration by a moving average window to reduce the introduction of artifacts and small-scale features.

Active seismic shot data are weighted equally with earthquake arrivals during the solving process through the residuals of their onset time, but they naturally carry additional information. The source locations and origin times of shot data are known and their waveforms often contain higher frequencies that may allow smaller picking uncertainties than those from earthquakes. This naturally weights shot data more, because solving for their residuals will only perturb the model wave speeds.

A fine-grid spacing of 250 m was employed based on the average seismic wavelength that was estimated for earthquakes within the geothermal field. This distance is certainly smaller than the expected model resolution. A variable horizontal grid spacing was chosen to approximately reflect our seismometer spacings at the surface. Tests were also performed with constant 1 km, 2 km, and 3 km wide grid nodes, which led to broadly similar velocity models. We use a variable depth spacing with finer depth intervals near the surface because of the higher density of earthquakes in the top 3 km. Ideally, an optimal selection of grid spacing allows the inversion to reduce the data variance down to the expected maximum data error.

The model roughness is often used as a diagnostic to determine an optimal damping parameter, which is found where the data misfit is greatly reduced with only a moderate increase in the model roughness [*Eberhart-Philips*, 1986; *Hansen*, 1992]. While this is critical for noniterative techniques, it is still useful here to decide whether one model is preferred over another in the case where the data fits are similar in both models. In such a case we choose the smoother model. Figure 2b (dashed line) shows the model roughness versus data misfit after five iterations for a range of damping values using only our earthquake data. The full curve (Figure 2b, solid black line) is shown for the damping parameter that led to our final earthquake model. An L-shaped curve is expected, confirming that the data contain coherent and statistically significant information [*Soldati et al.*, 2006]. We also tested different model smoothing windows (three, five, and seven nodes) and selected the three-node smoothing value for our inversion, because strong model smoothing hinders the inversion fitting the data. The inversion is halted when the variance and its standard deviation do not decrease significantly relative to previous iteration steps. Possible sources of bias in the consistency of the resulting models were evaluated by performing trial data inversions with three different 1-D starting models [*Arnott and Foulger*, 1994; *Brandsdóttir et al.*, 1997] and subsets excluding 10% or 20% of the data. We were able to retrieve the main structural features during all these trial runs.

The tomography code allows us to invert for V_p and V_s or for V_p and V_p/V_s directly. We expect the V_p model to show better spatial resolution than the V_s model, as we have more P wave than S wave arrival times and they usually have smaller picking uncertainties. Instead of solving for V_s, we directly invert for the *S-P* traveltime differences, because the velocity ratio is a good indicator of lithological and rheological changes in the rock. *P* wave velocities and V_p/V_s values are sensitive to the pore fluid content, pore pressure, crack density, crack aspect ratio, temperature, and chemical composition [e.g., *O'Connell and Budiansky*, 1974; *Ito et al.*, 1979; *Christensen*, 1996; *Nakajima et al.*, 2001]. In combination, V_p and V_p/V_s values are especially useful for geological interpretation of the models.

4. Model Results Using Our Earthquake Data Set

Specific cross sections of our V_p (left column) and V_p/V_s (right column) models are chosen for display in Figure 3 mostly because they are close to receivers. We describe only the coarse structures that show coherent velocity

anomalies, therefore minimizing the interpretation of small-scale tomographic artifacts. Local names mentioned in the following text are marked in Figure 9. Overall, the coarse (2–3 km) acoustic structure of the Krafla caldera is complex, having moderate seismic contrasts in both lateral and vertical directions. Anomaly A (Litla-Krafla) has a higher V_p structure of 2–3 km width that extends down and widens at about 2 km depth bsl. Higher velocities than the surrounding region are also imaged in region B (Graddabunga) from 0.5 km to at least 2 km depth bsl in Figure 3b. Furthermore, we see that several high-V_p bodies are mapped at about 2 km depth bsl (C, Figure 3). They are difficult to identify as separate bodies due to the smearing, as a recovery test discussed below shows. In contrast, a distinct low-V_p body (D), elongated E-W between Leirhnjúkur and the IDDP-1 well, is imaged at about 2 km depth bsl. When analyzing the velocity structure using isosurfaces of ≥ 4.9 km/s, two otherwise separated low-V_p bodies connect at about 2.5 km depth bsl.

In comparison, the V_p/V_s panels in Figure 3 show only three distinct bodies significantly deviating from $V_p/V_s = 1.76$: two low-V_p/V_s bodies and one high-V_p/V_s body. The shallow low-V_p/V_s feature (E, Leirhnjúkur, Figure 3l) extends from the surface to 0.0–0.5 km depth bsl. A deeper situated body (G) with $V_p/V_s \leq 1.67$ is centered at 2.0–2.5 km depth bsl. Higher V_p/V_s values (F, Leirbotnar) are calculated at intermediate (1.0–1.5 km bsl) depths. Note that we have not observed a second anomalous low-V_p/V_s region west of G, where low V_p values were also mapped at 2 km depth bsl. The real extent of these bodies described above may differ due to the tomographic parameterization (e.g., grid spacing and ray paths) and cannot be determined to an accuracy of less than the coarse-grid node spacing.

4.1. Synthetic Modeling
Stable solutions for our data inversion are most likely achieved in cells with a high ray coverage. Figure S1 in the supporting information provided in the supporting information, shows the ray coverage of Figure 3. P wave coverage is very good with some cells containing more than 1000 rays. S wave coverage is good in the center of the profiles, but poorer at the edges, leading to less stable solutions there. A majority of located earthquakes have hypocenters within the uppermost 3 km.

We perform tests with synthetic data to evaluate the spatial resolution and amplitudes of the model structures and to find optimal inversion parameterizations [*Koulakov et al.*, 2009]. In cases where the inverse problem is large, calculating the "resolution" matrix is unsuitable and we have to find other methods of assessing the model resolution. Checkerboards, for example, are commonly used to determine the amount of image blurring [e.g., *Zelt*, 1998]. We superimposed an alternating pattern of positive and negative V_p and V_p/V_s anomalies of $\pm 10\%$ on our starting model and calculated synthetic arrival times for the same phases and the same source-receiver configuration as in the real inversion run. The same picking errors applied to the real data were transferred to the corresponding synthetic arrival times and then inverted with the same free parameters and 1-D starting model as in the real case. We constructed the alternating pattern of high and low values with gaps between them to assess the smearing in recovered V_p and V_p/V_s values.

The rectangular patterns, superposed on the recovery results in Figure 4, represent nonlimiting columns perpendicular to the profiles. In the background, we show the percentage deviation of the initial model from the final model. Most V_p anomalies are well recovered in the center of the model. However, we observe diagonal smearing between the patterns, which is probably linked to the dominant ray directions. These tests also show that we experience some difficulty in resolving features near the surface at −0.5 to 0.5 km depth bsl (e.g., Figure 4m), where recovery is imperfect. This is likely to be caused by relatively coarse station spacing in some regions. Recovery of the V_p/V_s checkerboard amplitudes was more difficult due to the lower ray coverage. Nonetheless, most patterns in the center and top 4 km show a fair recovery giving us confidence to also interpret V_p/V_s anomalies.

Before we solved for the checker patterns and real data, we optimized the inversion parameters during the tests with synthetic data. Thus, synthetic and real data inversions were performed simultaneously. Recovery tests of the final model are shown later, where we also include shot data. However, the recovery results are very similar whether or not we include the shot data.

## 5. Model Results Further Including Data From Previous Studies

Here we discuss our earthquake data together with refraction data from *Brandsdóttir et al.* [1997]. A comparison between the large-scale V_p features imaged by *Arnott and Foulger* [1994] and ourselves show matching high-V_p structures beneath Litla-Krafla and Graddabunga, for example. Our orthogonal cross sections
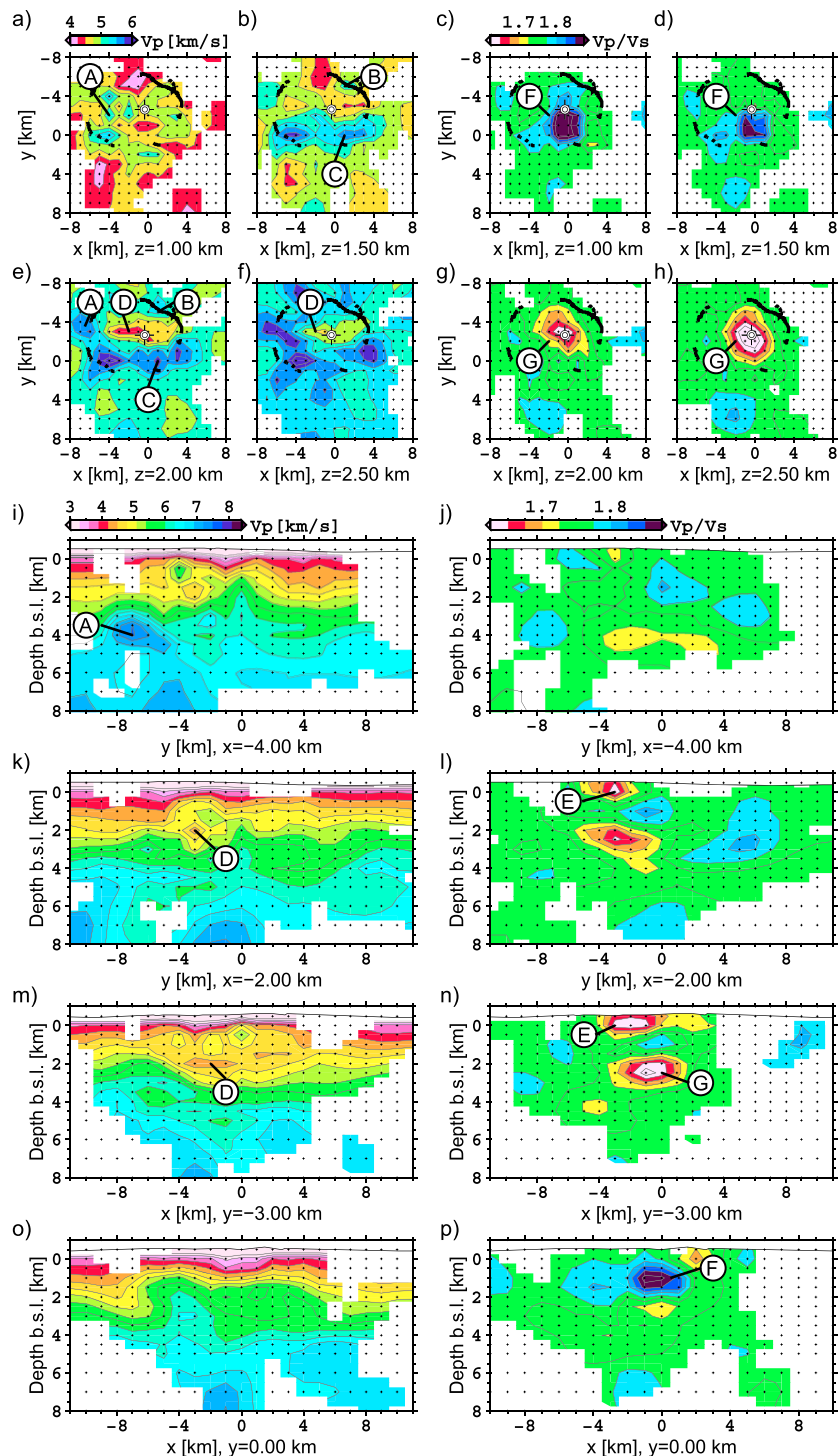
Figure 3. Selected cross sections in x, y, and z through the tomographic model. The figure shows slices of the (left column) V_p and (right column) V_p/V_s models. (a–h) Depth slices and (i–p) cross sections. Color scales for the panels are given at their top. Note that the color scales of the depth slices and cross sections are different. Cells with fewer than five rays passing through them are muted. Coarse-grid nodes are indicated by small crosses, the IDDP-1 well with the crosshair symbol, and anomalies discussed in the text with capital letters. The mapped caldera rim is shown in Figures 3a–3h as curved solid black lines.
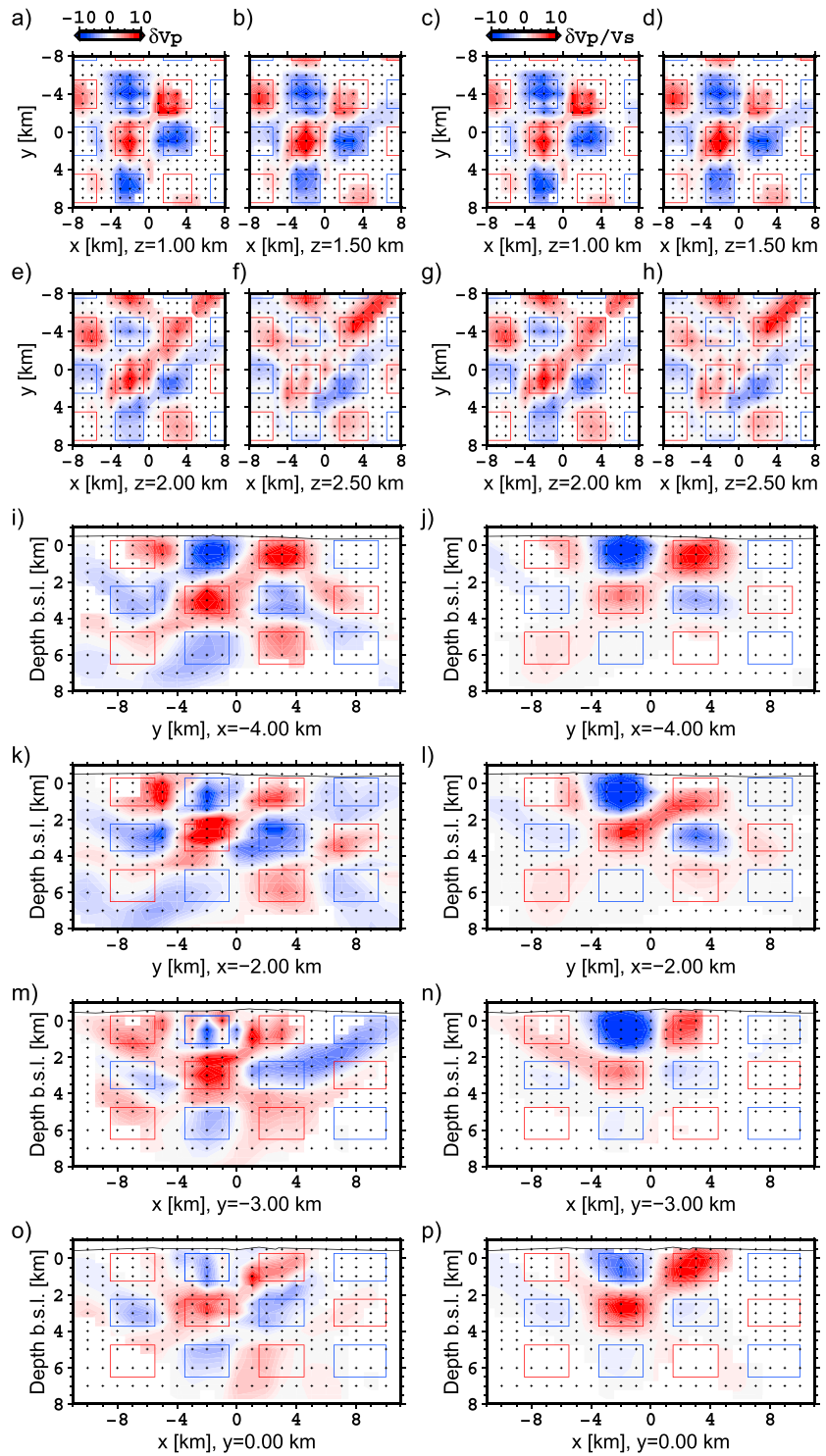
Figure 4. Reconstruction of checkerboard-like synthetic models using the V_p and V_p/V_s inversion scheme. The form of the superposed V_p and V_p/V_s anomalies (rectangles) represent horizontally and vertically nonlimited columns perpendicular to the cross sections. We imposed amplitude variations of $\pm 10\%$ on the initial starting velocity model. Coarse-grid nodes are indicated by small crosses. The coordinates of selected (a–h) depth slices and (i–p) cross sections are identical to those shown in Figure 3.
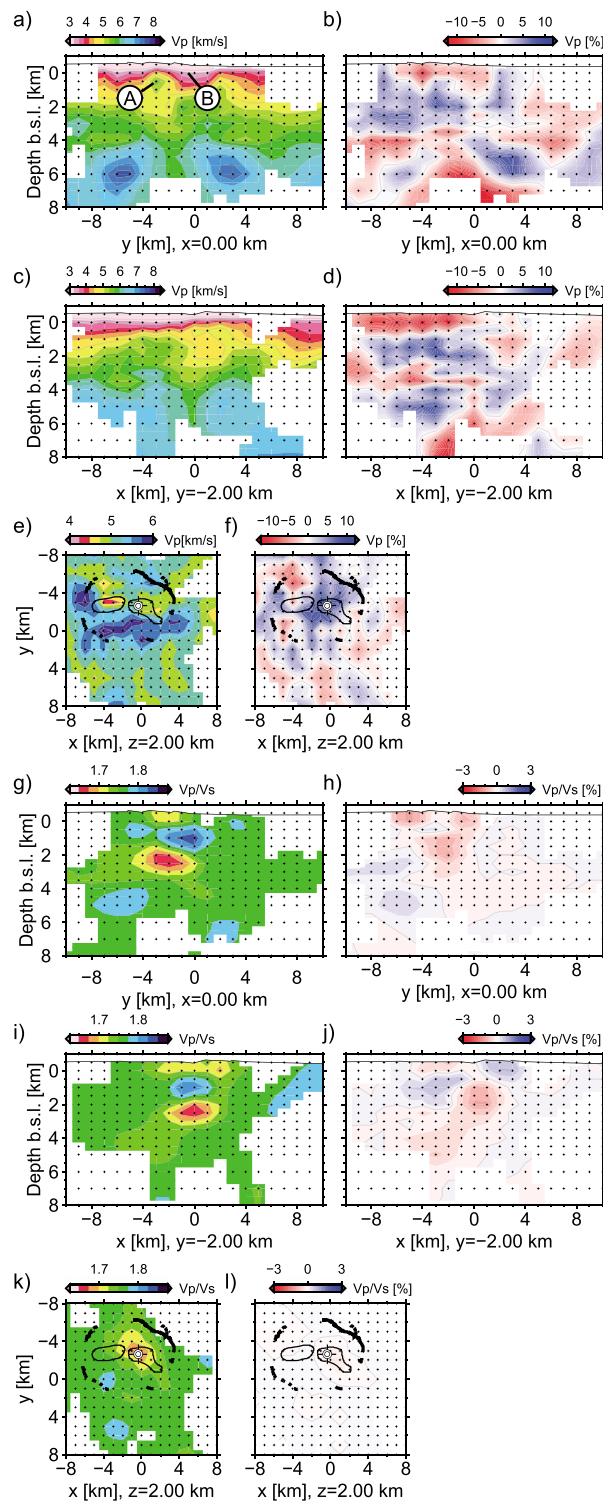
Figure 5. (a, c, g, and i) Cross sections of the tomographic model obtained using earthquake and shot data. (b, d, h, and j) The percentage deviation of this model compared to the result obtained using only earthquake data in the inversion. We observe in the V_p panels (Figures 5a–5f) that the shot data helped to better constrain the velocities in the shallow subsurface. Capital letters mark anomalies discussed in the text. S wave shadows (thin black lines) inside the caldera rim outlined by *Einarsson* [1978], the mapped caldera rim (thick black lines), and the IDDP-1 well as cross hair symbol are plotted in (e, f, k, and l) the depth cross sections.
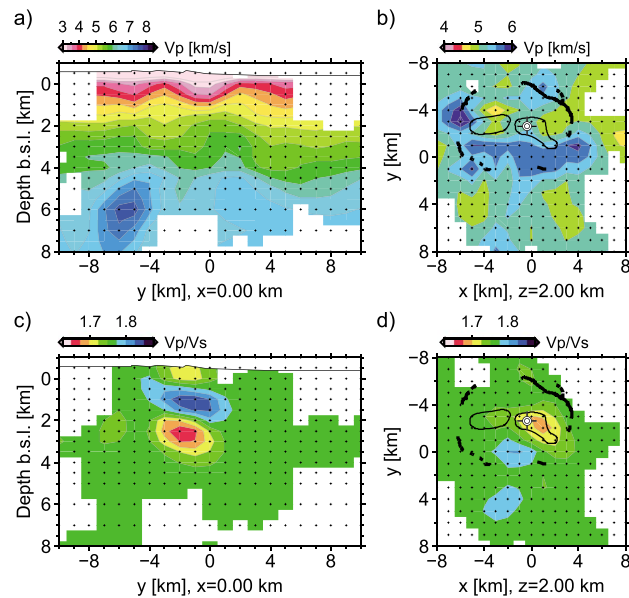
Figure 6. Real structure recovery test of (a,b) V_p and (c,d) V_p/V_s. The final tomographic model (Figure 5) was prepared as a synthetic model and the traveltimes then inverted with the same parameterizations and starting model as in the case with real data. Ideally, Figures 6a–6d should be identical to Figures 5a, 5e, 5g, and 5k, respectively.

(Figures 5a–5d) follow the NS and EW arrays of *Brandsdóttir et al.* [1997], crossing just west of the IDDP-1 bore-hole. Figure 5 (left column) displays the combined data inversion results, while Figure 5 (right column) gives the V_p and V_p/V_s model deviations from the inversion using only our earthquake arrivals. Overall, the same high- and low-V_p and V_p/V_s features are resolved. The refraction data further constrains near-surface velocities. In general, the combined model shows reduced V_p at shallow depths and slightly increased V_p underneath. For example, higher V_p velocities are observed at about 0.5 km depth beneath Krafla (A) compared to Hvíthólar (B) in Figures 5a and 6. Only small changes are observed between the V_p/V_s models with V_p/V_s contrasts becoming slightly weaker when including refraction data. An animation of the V_p/V_s anomalies in 3-D is provided in the supporting information (Figure S2).

5.1. Recovery Tests

Besides checkerboards, we attempt to recover a more realistic synthetic pattern to assess the stability of our solutions. As for the checkerboard tests, our final tomographic model (Figure 5) serves as an initial model to calculate synthetic traveltimes with the same hypocenter source distribution and picking errors copied from the real picks. These synthetic traveltimes are inverted with the same parameterization and 1-D starting model as used in the real case. Ideally, the real data model (Figures 5a, 5e, 5i, and 5k) should be identical to the recovered model in Figures 6a–6d. The prominent features in V_p and V_p/V_s velocity structures are well recovered. As mentioned earlier the real size of the anomalies may be smaller because of smearing, which can result in features appearing enlarged. To test the effects of smearing, we model a V_p/V_s anomaly at 2–3 km depth bsl beneath the Víti crater (Figures S3a and S3b, supporting information). The amplitude and relative shape of the imposed anomaly appears to be well recovered, giving us confidence in the interpretation. In another test shown in Figures S3c and S3d, we use high-V_p bodies that are connected at depth. These resemble high-V_p isosurfaces that possibly represent high-density and high-V_p intrusions beneath Litla-Krafla and south of Leirhnjúkur. Here we find that our resolution limit is 2 km and 0.5 km in horizontal and vertical directions, respectively, in the central caldera.

5.2. Earthquake Relocations and 1-D Velocity Profiles

Events incorporated in the final tomography run were further relocated using the *HypoDD2.1* double-difference algorithm by *Waldhauser and Ellsworth* [2000] and the hypocenters shown in Figures 7a and 7b. This procedure gives precise relative hypocenter locations of closely spaced events by reducing the error from unmodeled velocity variations between station and event pairs. Ray paths between stations and hypocenters are calculated with our final 3-D velocity model using an incorporated ray tracing algorithm [*Um and Thurber*, 1987]. Vertical and horizontal location uncertainties of the hypocenters, quoted from *HypoDD* using
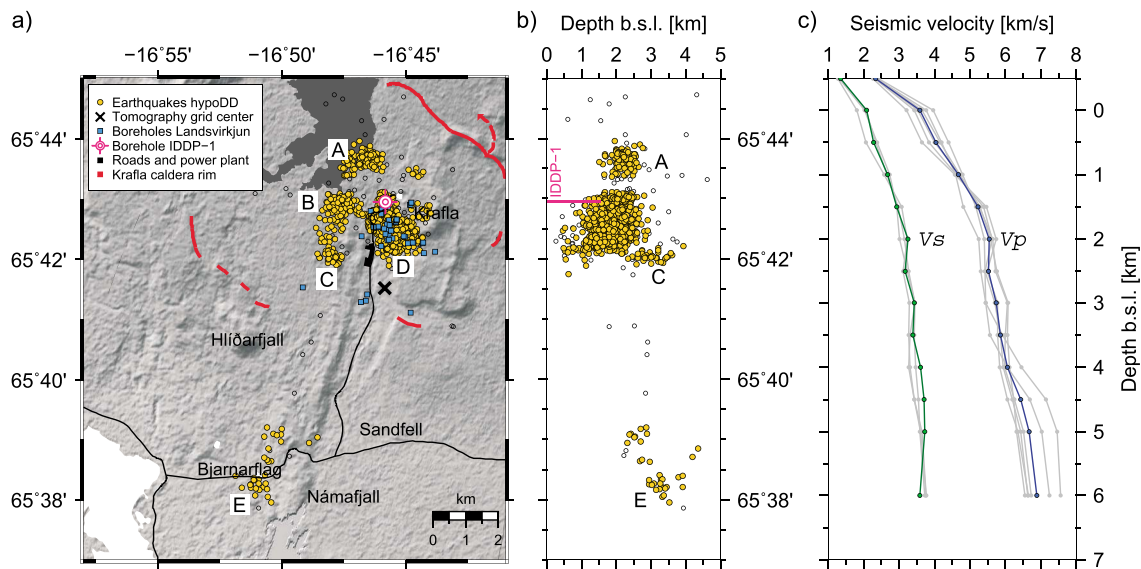
Figure 7. (a) Relocated earthquake locations using *HypoDD* and our final 3-D velocity model, (b) projected onto a north-south cross section. (c) Final averaged 1-D velocity models for V_p (blue) and V_s (green) based on the gray colored profiles. The profiles in gray color are selected after the criterion that all inversion cells (nodes) at a particular surface location to 6 km depth bsl have a minimum of 30 P wave and 20 S wave ray measurements at each depth level.

the singular-value-decomposition solver, are of the order of a few meters. We regard these uncertainties as minimum estimates since other error sources (e.g., velocity model uncertainties) are not included. Three distinct earthquake clusters, A, B, and C originate within the fissure swarm transecting Leirhnjúkur, Cluster A lies north and northeast of Leirhnjúkur, cluster B extends south from Leirhnjúkur, and C lies southwest Leirhnjúkur. Cluster C has a more confined depth range of 2.4–3.5 km bsl. Most earthquake hypocenters, however, cluster in the Leirbotnar-Suðurhlíðar area at depths less than 3 km bsl (Figure 7a, cluster D). Cluster E originates beneath the Bjarnarflag geothermal field. Furthermore, earthquakes located in clusters A, B, C, and E align well with the path of dike intrusions along the fissure zone activated during the Krafla fires. These events are most likely related to dike cooling and contraction from the rifting episode but may also be caused by geothermal activity.

In order to generate 1-D P and S wave velocity profiles from the combined earthquake and refraction data inversions (Figure 7c), we searched all grid nodes for velocity columns with a minimum of 30 P wave and 20 S wave ray paths. The mean velocities at each depth node are displayed in color, and the velocity profiles in gray color indicate the number of columns that fulfill our search criteria. The velocity profiles are from the area close to the Krafla geothermal area.

5.3. In Situ V_p/V_s Values

A Wadati diagram [*Wadati*, 1933; *Kisslinger and Engdahl*, 1973], i.e., S-P arrival time plotted versus P wave arrival time for an event, displays a straight line with a slope of ($V_p/V_s - 1$) when the seismic rays passed through a medium with constant V_p/V_s ratio. In reality, V_p/V_s changes spatially in the subsurface leading to scatter in the Wadati diagram, where the best fit line gives an estimate of the average V_p/V_s ratio of the medium sampled by the seismic rays. We calculated an average V_p/V_s of 1.76 using the earthquakes included in the tomography.

We estimated local V_p/V_s values from adjacent earthquake clusters using the method outlined by *Lin and Shearer* [2007]. The method follows the same assumptions as the double-difference relocation method. The standard deviation is estimated by a bootstrap approach [*Efron and Gong*, 1983], where the measurements are randomly resampled a hundred times before evaluation. The earthquakes used for the local V_p/V_s values of two earthquake clusters within the Leirbotnar-Suðurhlíðar region are presented in Figure 8. The background V_p/V_s model was interpolated from the tomographic model between the nearest cross sections ($x = 0$ km and $x = 2$ km) on either side of the IDDP-1 drill hole, where magma is expected to reside at shallow depth, so that the slice shows the most likely velocity model at the well site. There is good agreement between the V_p/V_s
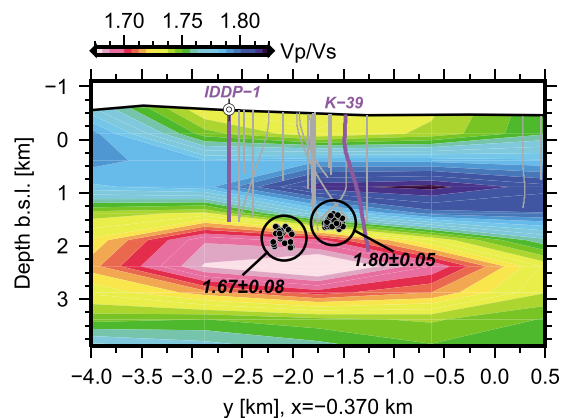
Figure 8. Trilinearly interpolated V_p/V_s model in cross section intersecting the IDDP-1 well site. The tomographic model was obtained using both earthquake and shot data. We display all wells that have their wellhead located within 300 m distance on either side of the cross section. IDDP-1 and KJ-39 are the only wells that drilled into rhyolitic melt. Two relocated hypocenter clusters used to calculate in situ V_p/V_s values are highlighted. They match the background model within their error bars.

values from the tomographic model and the local V_p/V_s values from the two earthquake clusters. However, note that the lower boundary of the low V_p/V_s anomaly at 2.5–3.0 km depth bsl is not as well constrained as the upper boundary where we have higher ray coverage.

The second well that entered magma, KJ-39, was directionally drilled eastward with a wellhead slightly offset (282 m at the top and 1355 m at the bottom) from the plane displayed in Figure 8. The consistency between the earthquake clusters and the V_p/V_s values from the models gives us confidence that the strong V_p/V_s changes between 1.5 and 2.0 km bsl are correct. We interpret their causes in the next section.

6. Discussion

Multiple factors (e.g., rock types, porosity, permeability, chemical alteration, temperature, and fluid pressure) affect the velocities of seismic waves propagating through the subsurface [*Wang*, 2001], especially in a heterogeneous volcanic setting such as Krafla. In general, *P* and *S* wave velocities rise with increased effective pressures [e.g., *Winkler*, 1985] and fall with increasing temperatures [e.g., *Timur*, 1977; *Wang*, 1988]. At the onset of partial melting, V_s decreases rapidly relative to V_p [*Mizutani and Kanamori*, 1964]. In addition, velocities vary significantly between rock types. High seismic velocities are usually attributed to intrusive rocks (e.g., gabbro and dolerite) formed during slow cooling of magma. Extrusive rocks, such as hyaloclastites or basalt flows, tend to have lower velocities due to vesicles and secondary minerals embedded in the rock matrix [*Schuler*, 2014]. However, hyaloclastites have considerably lower permeability than porous basalts and can serve as a cap rock in geothermal areas [*Alfredsson et al.*, 2013].

6.1. Velocity Structure of the Krafla Caldera

We observe localized high-V_p regions at about 1 km depth bsl near the caldera rims (Figure 3, anomalies A–C). Most prominent is an east-west trending high-V_p body (anomaly C) along the southern caldera rim, which becomes more extensive with increasing depth. Characterization of the deeper parts of anomaly C is, however, uncertain, since we do not have good resolution at such short spatial scales (Figure 6b). We interpret the high-V_p regions as representing dense intrusives injected into the shallow crust. This is supported by borehole data with an intrusive complex below 800 m depth bsl in the IDDP-1 [*Mortensen et al.*, 2014] and other boreholes in the Leirbotnar-Suðurhlíðar region [*Mortensen et al.*, 2010] deepening to 1.1 km depth bsl along the southern caldera rim, by Hvíthólar [*Ármannsson et al.*, 1987].

Shallow low-V_p anomalies are observed at 1.0–1.5 km depth bsl, south and east of the IDDP-1 borehole, in the northern part of the caldera (beneath Rauðkollur) and south of Hlíðarfjall (Figures 3a, 3b, and 9). The caldera rim anomalies are less well constrained due to the relatively sparse station distribution in those regions. The low-V_p anomalies possibly represent basins filled with hyaloclastites and basalt extrusives similar to the uppermost sequences underneath Krafla. The Hlíðarfjall anomaly could also be associated with a rhyolitic dome at the SE caldera rim.
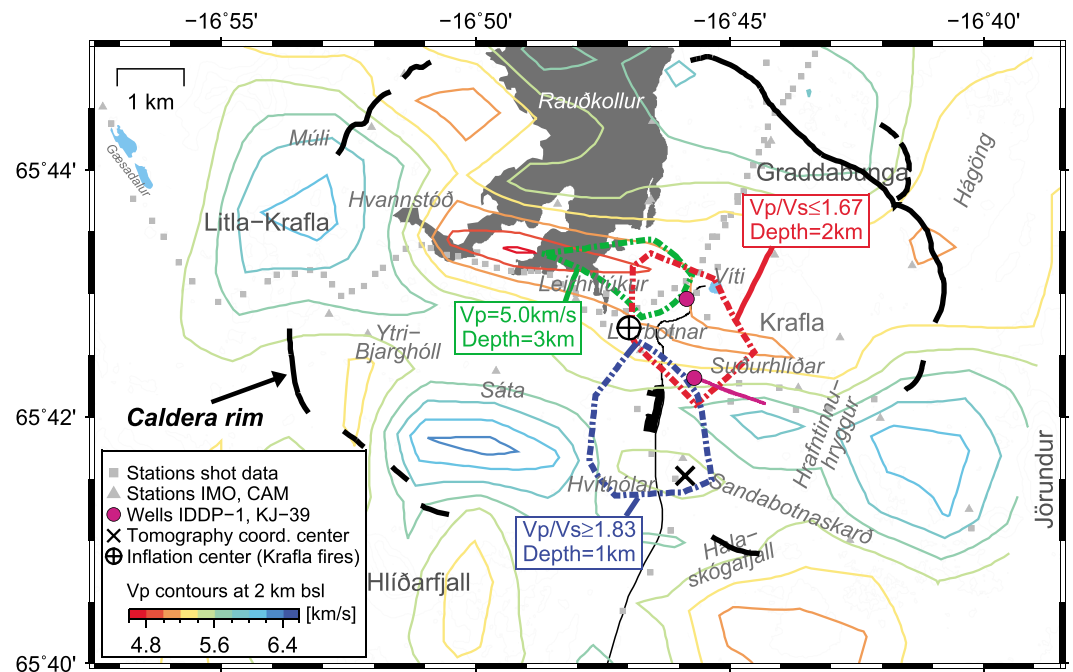
A distinct east-west trending low-V_p zone at 1.5–2.5 km depth bsl is observed beneath the IDDP-1 borehole, extending 4 km east and west of the well at 2 km depth bsl (anomaly D in Figures 3e, 3f and Figure 9) with V_p values as low as 4.4 km/s. Anomaly D extends down to 3.0–3.5 km depth bsl between Leirhnjúkur and Víti (Figure 9, green line) and closely matches the delineated surface locations of two attenuating bodies found by *Einarsson* [1978]. The top of the low-V_p anomaly beneath Víti is constrained by the IDDP-1 and KJ-39 wells at 1.6 km, where magma was encountered.

Figure 9. Colored V_p contour lines at 2.0 km depth bsl of the final tomographic model. Two high- and low-V_p/V_s anomalies are superimposed with dashed red and blue lines, respectively, and the low-V_p contour line at 3.0 km depth bsl is marked as a dashed green line. Symbols indicating the station locations (triangles), the wells (and trajectories) that drilled into magma (purple), inflation center measured from repeated ground leveling during the Krafla fires (cross in circle) [*Björnsson et al.*, 1985], and the local tomographic grid center are listed in the legend. The thin black lines indicate roads, the black patch the power plant. The mapped caldera rim is indicated by the thick black line.

Árnason et al. [2009] presented MT inversion results showing the top of two shallow conductors at about 2 km depth bsl beneath Víti and about 1 km NNE of Leirhnjúkur. They match our shallow low-V_p zone beneath Víti and our deeper low-V_p zone at 3.0 km depth bsl, but we note that no shallow conductor was found WNW of Leirhnjúkur.

6.2. V_p/V_s Anomalies

In a hydrothermal system, it is well known that saturation and fluids strongly affect the bulk modulus (V_p) whereas the shear modulus is insensitive to fluid inclusions [*Nur and Simmons*, 1969]; thus, we may use the V_p/V_s values as an indicator of the physical state of fluids in the pores. For example, *Winkler and Nur* [1982] measured higher V_p/V_s for brine-saturated rocks and lower V_p/V_s for gas-saturated rocks and brine-gas mixtures. *Ito et al.* [1979] showed how the saturation state affects the velocities and how V_p/V_s increases as pore pressure increases due to phase changes of the fluids from vapor to liquid. The phase changes depend on the temperature and fluid pressure. V_p/V_s values have been used as an indicator for phase changes to interpret results from geothermal reservoirs [e.g., *Delliansyah et al.*, 2015], but such values are probably best used with time lapse data where changes in the same reservoir are analyzed [e.g., *Gunasekera et al.*, 2003]. When comparing V_p/V_s values of reservoirs with different lithologies, crack porosity orientation and density may be important parameters that affect V_p/V_s. For example, we may observe low V_p/V_s values in cases where seismic waves are polarized perpendicular to the cracks.

Temperatures inferred from mineral alterations [*Stefánsson*, 1981; *Ármannsson et al.*, 1987] and obtained from borehole measurements [*Mortensen et al.*, 2014; *Friðleifsson et al.*, 2015] suggest that the reservoir can be separated at roughly 0.5 km depth bsl into distinct upper and lower reservoirs, which match well our near-surface low-V_p/V_s and deeper high-V_p/V_s ratio zones (Figure 8). In the upper reservoir, the fluid temperature follows the boiling point curve for about 100 m below the water table and is then almost isothermal at temperatures around 200°C from about −0.4 km to 0.5 km depth bsl, although the mineralogy suggests that there were higher temperatures in the past. Thus, the upper reservoir is likely to be liquid dominated and exhanges heat by convective flow through permeable rocks [*Stefánsson and Steingrímsson*, 1980]. The uppermost 100 m are probably steam dominated due to the low pore pressures and high fluid temperatures.

Lower measured temperatures and higher expected porosities and fractures characterize the shallow relative to the deeper reservoir. We surmise that an abundance of fractures and pores filled with hot water are the dominating factors that cause the observed low-V_p/V_s values in the shallow reservoir. *Dvorkin et al.* [1999] reported that lower V_p/V_s values are expected for rocks with higher crack porosities.

Intrusives were encountered below 0.5 km depth bsl; thus, lower porosities and permeabilities are expected for the deeper reservoir [*Mortensen et al.*, 2014]. Here temperatures follow the boiling point curve up to 300–350°C between 0.5 and 1.5 km depth bsl, which means that the reservoir is a liquid-vapor phase fluid system. It is likely that heat is vertically exchanged by counterflow, where liquid trickles down and steam rises. *Markusson and Hauksson* [2015] reported that alkaline brine is feeding the IDDP-1 well between 0.25 and 1.25 km depth bsl. The upper depth intervals are cased. We resolved a high-V_p/V_s zone between 0.5 and 1.5 km depth bsl (dashed blue line in Figure 9 and Figures 5g and 5i). Our findings differ in this depth interval from those of *Parker* [2012], whose strong low-V_p/V_s zone extends to 1.5–2.0 km depth bsl. Recovery tests performed with and without shot data encourage us to interpret the high V_p/V_s anomaly as a real feature required by the data (Figure 5g or 8). We surmise that the fluid saturation of the rocks in the reservoirs may have a smaller impact on V_p/V_s values than the impact of the porosities and crack densities, because otherwise we would expect higher V_p/V_s values for a fully liquid-saturated upper reservoir compared to a liquid-gas-saturated deeper reservoir. The high V_p/V_s anomaly around 750–800 m depth bsl (Figure 8) correlates with the interface between the extrusives and basaltic dyke sequence in the boreholes KJ-39 and IDDP-1 [*Mortensen et al.*, 2010, 2014], which were drilled close to the center of the anomaly (Figure 9).

Close to the magma body, which is expected to be at 900°C, superheated steam rich in hydrogen chloride and with temperatures above 450°C is feeding the well below 1.45 km depth bsl [*Friðleifsson et al.*, 2015; *Markusson and Hauksson*, 2015]. Here below the deeper reservoir, we mapped another low-V_p/V_s anomaly. We highlighted $V_p/V_s = 1.67$ at 2.0 km depth bsl in Figure 9 for orientation. Other studies in volcanic areas have proposed that their low V_p/V_s values are due to the presence of rhyolitic or volatile-rich magmas [e.g., *Husen et al.*, 2004; *Patanè et al.*, 2006; *Zhang and Lin*, 2014]. We suggest that our low-V_p/V_s (≤ 1.65) zone at 2–3 km depth bsl beneath Víti is linked to the thin superheated steam zone overlying melt and/or the rhyolitic magma intrusion itself. Figure 8 shows a smooth, rather than sharp, V_p/V_s contrast at 1.6 km depth bsl. The smoothness comes from the trilinear interpolation of our 0.5 km vertical grid spacing. An algorithm that could adapt the grid cell sizes during the data inversion might resolve a sharper V_p/V_s contrast.

Christensen [1996] suggested that V_p/V_s decreases with increasing silica content in rocks and quartzite would have a V_p/V_s of 1.48 at this depth. We know, however, that IDDP-1 encountered felsite without melt (subsolidus temperature) before entering magma. The most productive zone for injecting fluids into the formation at the bottom of IDDP-1 apparently lies within the subsolidus felsite, which produced dry superheated steam at the wellhead [*Mortensen et al.*, 2014; *Friðleifsson et al.*, 2015]. Thus, our low-V_p/V_s values may be explained by a highly fractured rock, bearing superheated steam in its pores and cracks, or from a felsic crystal-rich magma that contains an abundance of vapor bubbles in situ, or both. The low amounts of exsolved bubbles in the quenched glass retrieved from IDDP-1 suggest that the felsic melt has partially degassed [*Zierenberg et al.*, 2012]. To our knowledge, no laboratory measurements comparing V_p/V_s of porous fractured rock with dense, volatile-rich partial melt yet exist at the pressure and temperature conditions experienced at Krafla.

Close to the melting point, both *P* and *S* wave velocities decrease rapidly [*Mizutani and Kanamori*, 1964]. While V_s trends to zero in melt, V_p values remain higher in liquids and thus high V_p/V_s values can be measured in the presence of partial melt. Considering a sufficiently small magma body, *S* waves may still be recorded, albeit delayed in time, on the opposite side of the body since the *S* waves may travel around the magma pocket. We speculate that the low-V_p/V_s values are mostly caused by the superheated steam zone. Note that we necessarily extrapolated laboratory measurements of *Ito et al.* [1979], for example, to reach our temperature range. The superheated steam zone is expected to show high crack porosity and permeability, leading to lower V_p/V_s values, due to its productivity.

7. Conclusions

We present an improved seismic model of V_p and V_p/V_s beneath the Krafla caldera using earthquake and active seismic data. The tomographic results show prominent high-V_p bodies at intermediate (0.5–1.5 km) depths bsl beneath areas with higher topographic relief, which may indicate high-density intrusions. Relatively low-V_p values were mapped at shallow depths in the caldera and are associated with postglacial eruptive products.

Two more distinct low-V_p anomalies are imaged at 2–3 km depth bsl under Víti and east of Hvannstóð. The anomalies match the surface extent of the two attenuating bodies inferred from S wave shadows during the Krafla fires [*Einarsson*, 1978]. Furthermore, we mapped three distinct zones in the V_p/V_s model beneath the Leirbotnar geothermal field at Krafla. The shallow low-V_p/V_s and deeper high-V_p/V_s zones are interpreted as having different velocity ratios due to higher and lower porosity and crack densities, respectively. They match well the upper and lower geothermal reservoirs constrained by borehole measurements. Underneath the geothermal field, very low-V_p/V_s values are resolved close to where two boreholes drilled into ryholitic magma. We propose that the low-V_p/V_s region is associated with the superheated steam layer, which lies between the host rock and the felsic melt.

References

Ágústsdóttir, T., M. Gudmundsson, and P. Einarsson (2011), A gravity study of silicic domes in the Krafla area, N-Iceland, *Jokull*, *60*, 135–148.

Alfredsson, H. A., E. H. Oelkers, B. S. Hardarson, H. Franzson, E. Gunnlaugsson, and S. R. Gislason (2013), The geology and water chemistry of the Hellisheidi, SW-Iceland carbon storage site, *Int. J. Greenhouse Gas Control*, *12*, 399–418.

Ali, S. T., K. L. Feigl, B. B. Carr, T. Masterlark, and F. Sigmundsson (2014), Geodetic measurements and numerical models of rifting in Northern Iceland for 1993–2008, *Geophys. J. Int.*, *196*, 1267–1280.

Árnason, K., R. Karlsdóttir, H. Eysteinsson, Ó. G. Flovenz, and S. T. Gudlaugsson (2008), The resistivity structure of high-temperature geothermal systems in Iceland, in *Short Course III on Exploration for Geothermal Resources*, pp. 1–11, United Nations Univ., Kenya.

Árnason, K., A. M. Vilhjálmsson, and T. Björnsdóttir (2009), A study of the Krafla volcano using gravity, micro-earthquake and MT data, in *Short Course IV on Exploration for Geothermal Resources*, pp. 1–14, United Nations Univ., Kenya.

Arnott, S. K., and G. R. Foulger (1994), The Krafla spreading segment, Iceland 1: Three-dimensional crustal structure and the spatial and temporal distribution of local earthquakes, *J. Geophys. Res.*, *99*, 23,801–23,825.

Ármannsson, H., B. Gudmundsson, and B. S. Steingrímsson (1987), Exploration and development of the Krafla geothermal area, *Jokull*, *37*, 13–29.

Beblo, M., K. Björnsson, K. Arnason, B. Stein, and P. Wolfgram (1983), Electrical conductivity beneath Iceland—Constraints imposed by magnetotelluric results on temperature, partial melt, crust and mantle structure, *J. Geophys.*, *53*, 16–23.

Björnsson, A. (1985), Dynamics of crustal rifting in NE Iceland, *J. Geophys. Res.*, *90*, 10,151–10,162.

Björnsson, A., K. Saemundsson, P. Einarsson, E. Tryggvason, and K. Grönvold (1977), Current rifting episode in north Iceland, *Nature*, *266*, 319–322.

Björnsson, A., G. Johnsen, S. Sigurdsson, and G. Thorbergsson (1979), Rifting of the plate boundary in North Iceland 1975–1978, *J. Geophys. Res.*, *84*, 3029–3038.

Björnsson, A., G. Björnsson, Á. Gunnarsson, and G. þorbergsson (1985), Land elevation changes at Krafla, 1974–1984 [in Icelandic], *National Energy Authority Rep. OS-85019/JHD-05*, Natl. Energy Auth.

Brandsdóttir, B., and P. Einarsson (1979), Seismic activity associated with the September 1977 deflation of the Krafla central volcano in northeastern Iceland, *J. Volcanol. Geotherm. Res.*, *6*, 197–212.

Brandsdóttir, B., and W. H. Menke (1992), Thin low-velocity zone within the Krafla caldera, NE-Iceland attributed to a small magma chamber, *Geophys. Res. Lett.*, *12*(24), 2381–2384.

Brandsdóttir, B., and W. H. Menke (2008), The seismic structure of Iceland, *Jokull*, *58*, 17–34.

Brandsdóttir, B., W. Menke, P. Einarsson, R. S. White, and R. K. Staples (1997), Färoe-Iceland Ridge Experiment 2. Crustal structure of the Krafla central volcano, *J. Geophys. Res.*, *102*, 7867–7886.

Buck, W. R., P. Einarsson, and B. Brandsdóttir (2006), Tectonic stress and magma chamber size as controls on dike propagation: Constraints from the 1975–1984 Krafla rifting episode, *J. Geophys. Res.*, *111*, B12404, doi:10.1029/2005JB003879.

Christensen, N. I. (1996), Poisson's ratio and crustal seismology, *J. Geophys. Res.*, *101*, 3139–3156.

Constable, S. (2006), SEO3: A new model of olivine electrical conductivity, *Geophys. J. Int.*, *166*, 435–437.

Darbyshire, F. A., K. F. Priestley, R. S. White, R. Stefánsson, G. B. Gudmundsson, and S. S. Jakobsdóttir (2000), Crustal structure of central and northern Iceland from analysis of teleseismic receiver functions, *Geophys. J. Int.*, *143*, 163–184.

Delliansyah, R., R. Sule, and A. D. Nugraha (2015), Steam and brine zones prediction inside an operated geothermal reservoir based on seismic velocities produced by double difference tomography, paper presented at World Geothermal Congress 2015 Melbourne, Australia, 19–25 April 2015.

Drew, J., R. S. White, F. Tilmann, and J. Tarasewicz (2013), Coalescence microseismic mapping, *Geophys. J. Int.*, *195*(3), 1773–1785.

Dvorkin, J., G. Mavko, and A. Nur (1999), Overpressure detection from compressional- and shear-wave data, *Geophys. Res. Lett.*, *26*, 3417–3420.

Eberhart-Philips, D. (1986), Three-dimensional velocity structure in Northern California coast ranges from inversion of local earthquake arrival times, *Bull. Seismol. Soc. Am.*, *76*(4), 1025–1052.

Efron, B., and G. Gong (1983), A leisurely look at the bootstrap, the jackknife, and cross-validation, *Am. Stat.*, *37*, 36–48.

Einarsson, P. (1978), S-wave shadows in the Krafla caldera in NE-Iceland, evidence for a magma chamber in the crust, *Bull. Volcanol.*, *41*, 187–195.

Einarsson, P. (1991), Earthquakes and present-day tectonism in Iceland, *Tectonophysics*, *189*, 261–279.

Einarsson, P. (2008), Plate boundaries, rifts and transforms in Iceland, *Jokull*, *58*, 35–58.

Elders, W., et al. (2011), Origin of a rhyolite that intruded a geothermal well while drilling at the Krafla volcano, *Geology*, *39*, 231–234.

Friðleifsson, G. O., B. Pálsson, A. L. Albertsson, B. Stefánsson, E. Gunnlaugsson, J. Ketilsson, and P. Gíslason (2015), IDDP-1 drilled into magma—World's first magma-EGS system created, paper presented at World Geothermal Congress 2015, Melbourne, Australia.

Grönvold, K. (1976), Variation and origin of magma types in the Namafjall area, North Iceland, *Bull. Soc. Geol. Fr.*, *7*, 869–870.

Gunasekera, R. C., G. R. Foulger, and B. R. Julian (2003), Reservoir depletion at The Geysers geothermal area, California, shown by four-dimensional seismic tomography, *J. Geophys. Res.*, *108*(B3), 2134, doi:10.1029/2001JB000638.

Halldórsdóttir, S., H. Björnsson, A. K. Mortensen, G. Axelsson, and Á. Guðmundsson (2010), Temperature model and volumetric assessment of the Krafla geothermal field in N-Iceland, paper presented at World Geothermal Congress 2015, Bali, Indonesia.

Hansen, P. C. (1992), Analysis of discrete ill-posed problems by means of the L-curve, *SIAM Rev.*, *34*, 561–580.

Hjartardóttir, Á. R., P. Einarsson, E. Bramham, and T. J. Wright (2012), The Krafla fissure swarm, Iceland, and its formation by rifting events, *Bull. Volcanol.*, *74*, 2139–2153.

Hjartardóttir, Á. R., P. Einarsson, S. Magnúsdóttir, Þ. Björnsdóttir, and B. Brandsdóttir (2015), Fracture systems of the Northern Volcanic Rift Zone, Iceland: An onshore part of the Mid-Atlantic plate boundary, in *Magmatic Rifting and Active Volcanism*, edited by T. J. Wright et al., *Geol. Soc. London, Spec. Publ.*, 1–18.

Hole, J. A., and B. C. Zelt (1995), 3-D finite-difference reflection traveltimes, *Geophys. J. Int.*, *121*, 427–434.

Hollingsworth, J., S. Leprince, F. Ayoub, and J.-P. Avouac (2012), Deformation during the 1975–1984 Krafla rifting crisis, NE Iceland, measured from historical optical imagery, *J. Geophys. Res.*, *117*, B11407, doi:10.1029/2012JB009140.

Husen, S., R. B. Smith, and G. P. Waite (2004), Evidence for gas and magmatic sources beneath the Yellowstone volcanic field from seismic tomographic imaging, *J. Volcanol. Geotherm. Res.*, *131*, 397–410.

Ito, H., J. de Vilbiss, and A. Nur (1979), Compressional and shear waves in saturated rock during water-steam transition, *J. Geophys. Res.*, *84*, 4731–4735.

Jancin, M., K. D. Young, B. Voight, J. L. Aronson, and K. Saemundsson (1985), Stratigraphy and K/Ar ages across the west flank of the northeast Iceland axial rift zone, *J. Geophys. Res.*, *7*, 9961–9985.

Jónasson, K. (1994), Rhyolite volcanism in the Krafla central volcano, north-east Iceland, *Bull. Volcanol.*, *56*, 516–528.

Jónasson, K. (2007), Silicic volcanism in Iceland: Composition and distribution within the active volcanic zones, *J. Geodyn.*, *43*, 101–117.

Kisslinger, C., and E. R. Engdahl (1973), The interpretation of the Wadati diagram with relaxed assumptions, *Bull. Seismol. Soc. Am.*, *63*, 1723–1736.

Koulakov, I., T. Yudistira, B.-G. Luehr, and Wandono (2009), P, S velocity and V_p/V_s ratio beneath the Toba caldera complex (Northern Sumatra) from local earthquake tomography, *Geophys. J. Int.*, *177*, 1121–1139.

Lin, G., and P. Shearer (2007), Estimating local Vp/Vs ratios within similar earthquake clusters, *Bull. Seismol. Soc. Am.*, *97*, 379–388.

Lomax, A., J. Virieux, P. Volant, and C. Berge (2000), Probabilistic earthquake location in 3D and layered models: Introduction of a Metropolis-Gibbs method and comparison with linear locations, in *Advances in Seismic Event Location*, edited by C. H. Thurber and N. Rabinowitz, pp. 101–134, Kluwer Acad., Amsterdam.

Lomax, A., A. Michelini, and A. Curtis (2009), Earthquake location, direct, global-search methods, in *Encyclopedia of Complexity and System Science*, edited by R. A. Meyers, pp. 2449–2473, Springer, New York.

Maclennan, J. (2008), Concurrent mixing and cooling of melts under Iceland, *J. Petrol.*, *49*, 1931–1953.

Markusson, S. H., and T. Hauksson (2015), Utilization of the hottest well in the world, IDDP-1 in Krafla, paper presented at World Geothermal Congress 2015, Melbourne, Australia.

Metzger, S., S. Jónasson, G. Danielsen, S. Hreinsdóttir, F. Jouanne, D. Giardini, and T. Villemin (2013), Present kinematics of the Tjornes Fracture Zone, North Iceland, from campaign and continuous GPS measurements, *Geophys. J. Int.*, *192*, 441–455.

Mizutani, H., and H. Kanamori (1964), Variation of elastic wave velocity and attenuative property near the melting temperature, *J. Phys. Earth*, *12*, 43–49.

Mortensen, A. K., Þ. Egilson, B. Gautason, S. Árnadóttir, and Á. Guðmundsson (2014), Stratigraphy, alteration mineralogy, permeability and temperature conditions of well IDDP-1, Krafla, NE-Iceland, *Geothermics*, *49*, 31–41.

Mortensen, A. K., K. Grönvold, Á. Gudmundsson, B. Steingrímsson, and T. Egilson (2010), Quenched silicic glass from well KJ-39 in Krafla, north-eastern Iceland, paper presented at World Geothermal Congress 2010, Bali, Indonesia.

Nakajima, J., T. Matsuzawa, A. Hasegawa, and D. Zhao (2001), Three-dimensional structure of V_p, V_s, and V_p/V_s beneath northeastern Japan: Implications for arc magmatism and fluids, *J. Geophys. Res.*, *106*, 21,843–21,857.

Nur, A, and G. Simmons (1969), The effect of saturation on velocity in low porosity rocks, *Earth Planet. Sci. Lett.*, *7*, 183–193.

O'Connell, R. J., and B. Budiansky (1974), Seismic velocities in dry and saturated cracked solids, *J. Geophys. Res.*, *79*, 5412–5426.

Paige, C. C., and M. A. Saunders (1982), LSQR: An algorithm for sparse linear equations and sparse least squares, *ACM Trans. Math. Software*, *8*, 43–71.

Parker, B. S. (2012), Geophysical imaging methods for analysis of the Krafla geothermal field, NE Iceland, MSc thesis, Massachusetts Inst. Technol., Mass.

Patanè, D., G. Barberi, O. Cocina, P. de Gori, and C. Chiarabba (2006), Time-resolved seismic tomography detects magma intrusions at mount Etna, *Science*, *313*, 821–823.

Roecker, S., C. Thurber, K. Roberts, and L. Powell (2006), Refining the image of the San Andreas Fault near Parkfield, California using a finite difference travel time computation technique, *Tectonophysics*, *426*, 189–205.

Rymer, H., J. Cassidy, C. A. Locke, and F. Sigmundsson (1998), Post-eruptive gravity changes from 1990 to 1996 at Krafla volcano, Iceland, *J. Volcanol. Geotherm. Res.*, *87*, 141–149.

Sæmundsson, K. (1974), Evolution of the axial rifting zone in Northern Iceland and the Tjörnes Fracture Zone, *Geol. Soc. Am. Bull.*, *85*, 495–504.

Sæmundsson, K. (1979), Outline of the geology of Iceland, *Jokull*, *29*, 7–28.

Sæmundsson, K. (1982), Óskjur á virkum eldfjallasvæðum, (Calderas in the Neovolcanic zones of Iceland), in *Eldur er í nordri*, edited by H. Thórarinsdóttir, pp. 221–239, Festscrift for S. Thórarinsson, Reykjavík.

Sæmundsson, K. (1991), The geology of the Krafla Volcanic System (Jarðfræði Kröflukerfisins, in Icelandic), in *Náttúra Mývatns*, edited by A. Garðarsson and A. Einarsson, pp. 25–95, Hið íslenska náttúrufræðifélag, Reykjavík.

Schuler, J. (2014), Seismic wave propagation through flood basalts and stratigraphic correlation on the Faroes shelf, PhD thesis, Univ. of Cambridge, Cambridge, U. K.

Sigmarsson, O., J. Maclennan, and M. Carpentier (2008), Geochemistry of igneous rocks in Iceland: A review, *Jokull*, *58*, 139–160.

Sigmundsson, F., H. Vadon, and D. Massonnet (1997), Readjustment of the Krafla spreading segment to crustal rifting measured by Satellite Radar Interferometry, *Geophys. Res. Lett.*, *24*, 1843–1846.

Soldati, G., L. Boschi, and A. Piersanti (2006), Global seismic tomography and modern parallel computers, *Ann. Geophys.*, *49*, 977–986.

Staples, R. K., R. S. White, B. Brandsdóttir, W. Menke, P. K. H. Maguire, and J. H. McBride (1997), Fåroe-Iceland Ridge experiment 1. Crustal structure of northeastern Iceland, *J. Geophys. Res.*, *102*, 7849–7866.

Stefánsson, V., and B. Steingrímsson (1980), Production characteristics of wells tapping two phase reservoirs at Krafla and Námafjall, SGP–TR-50 presented at 6th Workshop Geothermal Reservoir Engineering, pp. 49–59, Stanford Univ., Stanford, Calif., 16–18 Dec.

Stefánsson, V. (1981), The Krafla geothermal field, Northeast Iceland, in *Geothermal Systems: Principles and Case Histories*, edited by L. Ryback and L. J. P. Muffler, pp. 273–294, John Wiley, Chichester.

Timur, A. (1977), Temperature dependence of compressional and shear wave velocities in rocks, *Geophysics*, *42*, 950–956.

Tuffen, H., and J. M. Castro (2009), The emplacement of an obsidian dyke through thin ice: Hrafntinnugryggur, Krafla Iceland, *J. Volcanol. Geotherm. Res.*, *185*, 352–366.

Um, J., and C. Thurber (1987), A fast algorithm for two-point seismic ray tracing, *Bull. Seismol. Soc. Am.*, *77*, 972–986.

Vidale, J. (1988), Finite-difference calculation of travel times, *Bull. Seismol. Soc. Am.*, *78*, 2062–2076.

Wadati, K. (1933), On the travel time of earthquake waves (Part II), *Geophys. Mag.*, *7*, 101–111.

Waldhauser, F., and W. L. Ellsworth (2000), A double-difference earthquake location algorithm: Method and application to the Northern Hayward Fault, California, *Bull. Seismol. Soc. Am.*, *90*, 1353–1368.

Wang, Z. (1988), Wave velocities in hydrocarbons and hydrocarbon saturated rocks—With applications to EOR monitoring, PhD thesis, Stanford Univ., Stanford.

Wang, Z. (2001), Fundamentals of seismic rock physics, *Geophysics*, *66*, 398–412.

Wendt, K., D. Möller, and B. Ritter (1985), Geodetic measurments of surface deformations during the present rifting episode in NE Iceland, *J. Geophys. Res.*, *90*, 10,163–10,172.

Winkler, K. W. (1985), Dispersion analysis of velocity and attenuation in Berea sandstone, *J. Geophys. Res.*, *90*, 6793–6800.

Winkler, K. W., and A. Nur (1982), Seismic attenuation: Effects of pore fluids and frictional sliding, *Geophysics*, *47*, 1–15.

Winpenny, B., and J. Maclennan (2014), Short length scale oxygen isotope heterogeneity in the Icelandic mantle: Evidence from plagioclase compositional zones, *J. Petrol.*, *55*, 2537–2566.

Wright, T. J., et al. (2012), Geophysical constraints on the dynamics of spreading centres from rifting episodes on land, *Nat. Geosci.*, *5*, 242–250.

Wyss, M., and J. N. Brune (1968), Seismic moment, stress, and source dimensions for earthquakes in the California-Nevada region, *J. Geophys. Res.*, *73*, 4681–4694.

Zelt, C. A. (1998), Lateral velocity resolution from three-dimensional seismic refraction data, *Geophys. J. Int.*, *135*, 1101–1112.

Zhang, Q., and G. Lin (2014), Three-dimensional V_p and V_p/V_s models in the Coso geothermal area, California: Seismic characterization of the magmatic system, *J. Geophys. Res. Solid Earth*, *119*, 4907–4922, doi:10.1002/2014JB010992.

Zierenberg, R. A., et al. (2012), Composition and origin of rhyolite melt intersected by drilling in the Krafla geothermal field, Iceland, *Contrib. Mineral. Petrol.*, *165*, 327–347.

Zverev, S. M., I. V. Litvinenko, G. Pálmason, G. A. Yaroshevskaya, N. N. Osokin, and M. A. Akhmetjev (1980), A seismic study of the rift zone in Northern Iceland, *J. Geophys.*, *47*, 191–201.